Spin textures of topological surface states at side surfaces of Bi_{2}Se_{3} from first principles

John W. Villanova and Kyungwha Park

Spin textures of topological surface states at side surfaces of Bi_2Se_3 from first principles

John W. Villanova and Kyungwha Park[*]

Department of Physics, Virginia Tech, Blacksburg, Virginia 24061, USA

(Dated: January 26, 2016)

Abstract

We investigate the spin and spin-orbital textures and electronic structures of topologically protected surface states at side surfaces of Bi_2Se_3 by using slab models within density-functional theory (DFT). This is motivated by recent experiments on nanowires, nanoribbons, and nanoplates of Bi_2Se_3 with side surfaces. In particular, two representative surfaces normal to the (111) surface, such as ($1\bar{1}0$) and ($11\bar{2}$) surfaces, are examined, in the presence of time-reversal symmetry and inversion symmetry. The ($1\bar{1}0$) surface lying in the mirror plane has twofold (C_2) rotational symmetry, whereas the ($11\bar{2}$) surface has only mirror symmetry. For the ($1\bar{1}0$) surface, we find that a Dirac cone with strongly anisotropic Fermi velocity is formed at Γ with the Dirac point at the Fermi level, and that the spin texture reveals features of Rashba-type combined with Dresselhaus-type spin-orbit coupling. For the ($11\bar{2}$) surface, a Dirac cone is found at either Γ or the Y point (along the mirror symmetry axis) below the Fermi level. In this case, the spin texture of the surface states strikingly differs from that of the (111) and ($1\bar{1}0$) surfaces: (i) the in-plane spin polarization dominantly aligned perpendicular to the [111] direction or the mirror symmetry axis, (ii) the Dresselhaus-like spin texture, and (iii) significant out-of-plane spin polarization away from the mirror symmetry axis. Our findings distinctively differ from the previous works based on the effective bulk model Hamiltonian. Our calculated spin and spin-orbital textures and band structures can be observed by spin-resolved angle-resolved photoemission spectroscopy.

PACS numbers: 73.20.At, 71.15.Mb

---

[*]Electronic address: `jwdvill@vt.edu,kyungwha@vt.edu`

I. INTRODUCTION

Symmetry-protected topological phases are interesting due to robustness of boundary states within a bulk band gap as long as a given symmetry is preserved. Two well-known examples are topological insulators (TIs) in the presence of time-reversal symmetry [1, 2] and topological crystalline insulators with mirror symmetry [3]. One class of the most studied three-dimensional TIs is the rhombohedral Bi_2Se_3 family with strong spin-orbit coupling (SOC). Along the crystal c axis, i.e., the [111] direction, atomic layers are arranged in units of quintuple layers (QLs) consisting of Se-Bi-Se-Bi-Se with ABC stacking [Fig. 1(a)] [4]. The thickness of one QL is about 1 nm. Neighboring QLs are bonded via weak van der Waals interactions, which facilitates exfoliation to create a (111) surface (or (0001) surface in the hexagonal lattice structure) and allows one to intercalate various neutral atoms within the van der Waals gap. Therefore, most studies of topologically protected surface states in the Bi_2Se_3 family have been carried out for the (111) surface. The previous theoretical and experimental works show an in-plane Rashba spin texture with interesting spin-orbital correlation in the vicinity of the Dirac point at Γ for the (111) surface [5–8].

Recently, nanoribbons and nanowires of Bi_2Se_3 family have been grown along the $[1\bar{1}0]$ direction (i.e., $[11\bar{2}0]_{\text{hex}}$), or along the [111] direction [9–12]. In the former case, the top and bottom surfaces correspond to (111) surfaces, while the side surfaces are $(11\bar{2})$ surfaces, where the $[11\bar{2}]$ direction corresponds to $[1\bar{1}00]_{\text{hex}}$. In the latter case, the top and bottom surfaces are $(1\bar{1}0)$ surfaces, and the side surfaces are $(11\bar{2})$ surfaces. See Fig. 1(a)-(c) for the overall directions and top views of the $(1\bar{1}0)$ and $(11\bar{2})$ surfaces, respectively. In addition, nanoplates of Bi_2Se_3 family have been fabricated with facets other than (111) [13]. Films of Bi_2Se_3 family with a (221) surface were also synthesized and their transport properties have been measured [14, 15]. Measurements of transport properties of the nanoribbons, nanowires, and nanoplates have shown strong anisotropy in electrical conductivity and in response to an external magnetic field, which is distinct from corresponding experiments on the (111) surface. Furthermore, at the side surfaces the outermost atomic layer contains both Bi and Se atoms, which would facilitate the possibility of either hole or electron doping by adsorption, whereas at the (111) surface adsorption mostly likely gives rise to electron doping due to the anionic nature of the outermost Se atomic layer.

Despite the interesting experiments on the side surfaces of the Bi_2Se_3 family, there are

2

much fewer theoretical studies on those side surfaces than on the (111) surface. The previous works [16–18] based on the effective model Hamiltonian treated all the normal surfaces to the (111) surface to be equivalent, and thus the spin textures of the $(1\bar{1}0)$ and $(11\bar{2})$ surfaces were shown to be identical. In these works, exclusion of higher order terms in the bulk Hamiltonian imparted continuous rotational symmetry to the (111) surface rather than the discrete symmetries actually present, and the surface reconstruction effect was absent.

In this work, we examine the spin and spin-orbital textures and electronic structures of topological surface states at the side or normal surfaces, such as $(1\bar{1}0)$ and $(11\bar{2})$ surfaces, by using relaxed slab models within density-functional theory (DFT). We find that the topological Dirac surface states for the two side surfaces have entirely different spin and spin-orbital textures from each other and from those of the (111) surface due to different symmetries of those side surfaces and the surface reconstruction. Our results are distinct from those of the literature [16–18]. For the $(1\bar{1}0)$-surface slab, a topological surface-state Dirac cone is formed at Γ ($k = 0$) with strongly anisotropic Fermi velocity, and the spin texture of the Dirac cone reveals Rashba-type features combined with Dresselhaus-type SOC. For the $(11\bar{2})$-surface slab, a Dirac point at either the Γ or Y point appears below the Fermi level E_{F}. Additionally, the spin texture of the Dirac cone for the $(11\bar{2})$ surface near Γ distinctively differs from that of the (111) and $(1\bar{1}0)$ surfaces: (i) The spin polarization is dominantly normal to the mirror symmetry axis; (ii) The upper Dirac cone reveals Dresselhaus-like spin texture, whereas the lower Dirac cone does not; (iii) There is a significant out-of-plane spin polarization except for the mirror symmetry axis. Our findings can be observed in spin-resolved angle-resolved photoemission spectroscopy.

We describe the symmetries of the $(1\bar{1}0)$ and $(11\bar{2})$ surfaces and reiterate the main differences between our approach and the method used in the literature, Refs.[16–18], in Sec.II. Then our slab geometries and the calculation method follow in Sec.III. The calculated results and analysis for the $(1\bar{1}0)$ and $(11\bar{2})$ slabs are separately presented in Secs.IV and V, respectively, since they show different spin textures and electronic structures. The differences between our results and the literature are also mentioned in Secs.IV and V. The conclusion is made in Sec.VI.
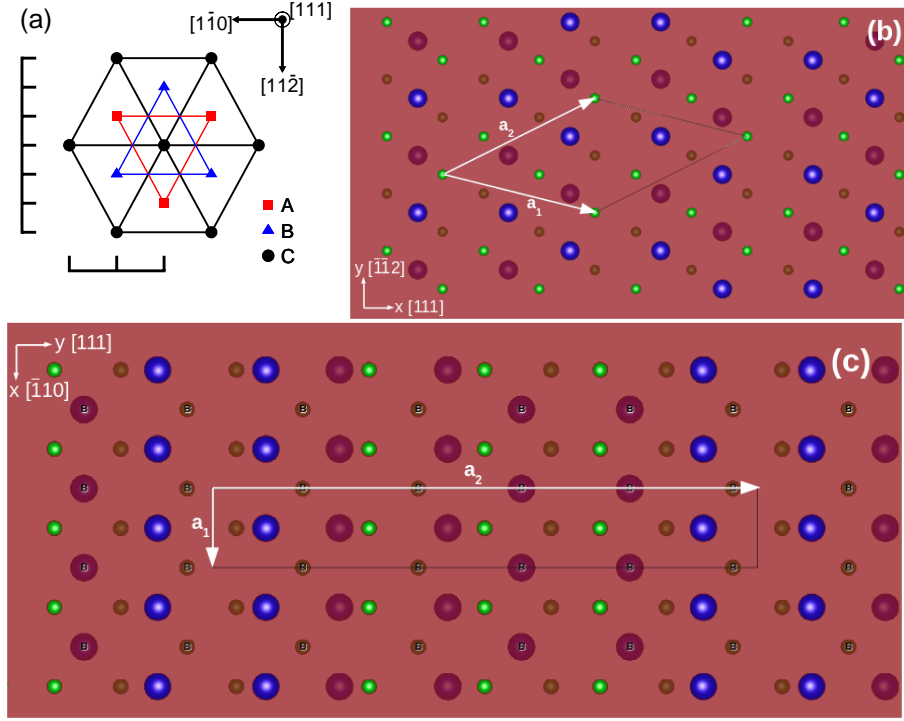
FIG. 1: (Color online) (a) Top view of bulk Bi_2Se_3 crystal along the crystal c axis. The bulk rhombohedral structure has ABC stacking that organizes into quintuple-layers Se-Bi-Se-Bi-Se. The stacking of the normal surfaces is emphasized by the hashed rulers on the left half of the figure. (b)-(c) Top views of $(1\bar{1}0)$ and $(11\bar{2})$ surfaces of Bi_2Se_3, which are normal to the (111) surface. Here $(1\bar{1}0)$ and $(11\bar{2})$ surfaces are equivalent to $(11\bar{2}0)$ and $(1\bar{1}00)$ in the hexagonal lattice, respectively. Large, blue circles are Bi and small, green circles are Se. $(1\bar{1}0)$ stacks with two inequivalent atomic layers in the unit cell and $(11\bar{2})$ stacks with six inequivalent atomic layers in the unit cell. In both cases, the topmost atomic layer is brightly colored, and in the latter case the second atomic layer is dull and labeled while the third atomic layer is merely dull. For $(11\bar{2})$, the three other inequivalent atomic layers are accessible by repeating the three shown atomic layers, but with a shift of $\frac{1}{2}\mathbf{a}_1$. In (b) and (c) the lattice vectors $\mathbf{a}_1$ and $\mathbf{a}_2$ are shown with the local x and y axes in the plane. (b) and (c) are drawn by using visualization program VESTA [19].

II.   SYMMETRIES OF SIDE SURFACES

To cleave the $(1\bar{1}0)$ and $(11\bar{2})$ surfaces, the chemical bonding between neighboring Bi and Se atoms must be broken. There is only one kind of surface termination for each side

surface. For both $(1\bar{1}0)$- and $(11\bar{2})$-surface slabs, the supercell or unit cell consists of two Bi and three Se atoms per atomic layer, as shown in the area confined by the lattice vectors (white arrows) in Fig. 1(b) and (c), respectively. Since the chemical bonding is broken, the surface reconstruction effect may be significant. However, each side surface is neutral in charge and thus passivating layers are not added to the slabs. Both slabs maintain time-reversal symmetry and inversion symmetry. Henceforth, the (x, y, z) coordinates are local coordinates rather than the crystal coordinates, unless specified otherwise; the z axis is selected to be perpendicular to the surface of interest.

The $(1\bar{1}0)$ slab has stacking in units of two atomic layers, as illustrated in Fig. 1(a). The x axis is chosen to be parallel to the [111] direction, as shown in Fig. 1(b). The $(1\bar{1}0)$ surface has C$_2$ symmetry about the z axis ($x \to -x$, $y \to -y$) and it lies in the mirror plane. The un-optimized $(1\bar{1}0)$ slab has perfect C$_2$ symmetry, which is only slightly broken upon surface reconstruction. For the $(11\bar{2})$ slab, we choose the y axis to be parallel to the [111] direction and the x axis to align along the [$\bar{1}10$] direction, as shown in Fig. 1(c). The $(11\bar{2})$ slab has stacking in units of six atomic layers, as illustrated in Fig. 1(a). The $(11\bar{2})$ surface has mirror symmetry across the y axis ($x \to -x$, $y \to y$), and this symmetry is retained even after geometry relaxation. Therefore, the $(1\bar{1}0)$ and $(11\bar{2})$ surfaces have distinct spatial symmetries.

We now compare the above spatial symmetries of the side surfaces with symmetries considered in the previous theoretical works [16–18]. In the literature, the spin textures of the side surfaces were derived starting from the effective bulk model Hamiltonian consisting of only linear and quadratic terms in momentum k. Higher-order terms than the quadratic terms were neglected in the model Hamiltonian. This simplification allows continuous rotational symmetry about the crystal c axis for the bulk and the (111) surface, implying that all normal surfaces to the (111) surface are identical in terms of symmetry. However, the bulk has only discrete symmetries [4] (rather than the continuous rotational symmetry), such as C$_3$ symmetry about the c axis, C$_2$ symmetry about the [$1\bar{1}0$] direction, and mirror symmetry about the $(1\bar{1}0)$ plane. See Fig. 1(a). The crystal symmetries can be properly addressed and incorporated in the side surfaces only when the higher-order terms in k are included in the model Hamiltonian prior to rotations of the spatial and spin coordinates. In contrast to the literature, our DFT calculations of the $(1\bar{1}0)$ and $(11\bar{2})$ slabs include the aforementioned correct discrete symmetries of the side surfaces as well as the surface reconstruction effect.

III. SLAB GEOMETRIES AND CALCULATION METHOD

We first construct the $(1\bar{1}0)$ and $(11\bar{2})$ slabs with thicknesses of 29 and 49 atomic layers, respectively, by using the bulk experimental lattice constants $a = 4.143$ and $c = 28.636$ Å [20]. For the $(1\bar{1}0)$ and $(11\bar{2})$ slabs, the distances between adjacent atomic layers are $a/2 = 2.0715$ Å and $\sqrt{3}a/6 = 1.196$ Å, respectively, before the geometry optimization or surface reconstruction. These slabs are equivalent to the $(1\bar{1}0)$ slab consisting of 14 units and an additional atomic layer and to the $(11\bar{2})$ slab comprising 8 units and one more atomic layer, respectively. We choose these thicknesses in order to keep inversion symmetry and to reduce the surface hybridization. Since both slabs have non-polar surfaces, we do not include passivating layers in the slabs. A vacuum layer of $4a$ (16.6 Å) is included in the supercell in order to avoid artificial interactions between neighboring supercells. The relaxed $(1\bar{1}0)$ and $(11\bar{2})$ slabs have thicknesses of 5.87 nm and 5.80 nm, respectively.

To relax the geometry and obtain band structures, we use a DFT code, `VASP` [21], within the Perdew-Burke-Ernzerhof generalized-gradient approximation (GGA) [22] for an exchange-correlation functional, with the projector-augmented-wave (PAW) pseudopotentials [23]. We take into account SOC in a self-consistent manner within DFT. A cutoff kinetic energy is set to 250 eV and the total energy converges down to 1×10^{-5} eV. For the $(1\bar{1}0)$ slab, the geometry is optimized by allowing the top nine and bottom nine atomic layers to relax until the maximum residual force is less than 0.1 eV/Å. The k-points of $7\times7\times1$ are sampled including Γ within the Monkhorst-Pack scheme. For the $(11\bar{2})$ slab, the geometry is optimized by allowing the top seven and bottom seven atomic layers to relax to the same force criterion. The k-points of $11\times3\times1$ are sampled including Γ within the Monkhorst-Pack scheme. For both surfaces, we check that our findings are not affected by further geometry relaxation with a more stringent force criterion, by relaxing more atomic layers, or by increasing the number of sampled k-points. At the examined thicknesses, hybridization between the top and bottom surface states is small, i.e. on the order of meV, for both slabs (for details, see Secs.IV and V).

The surface states are identified from our calculated band structures by examining electron density localization as a function of the z coordinate normal to a given surface. Surface states have electron density localized at the top or bottom surface within fifteen atomic layers by more than 80% for the $(1\bar{1}0)$ slab, or within ten atomic layers by more than 60%

for the $(11\bar{2})$ slab. Small changes of these criteria do not change our identification of the surface states.

IV. RESULTS AND DISCUSSION FOR $(1\bar{1}0)$ SURFACE

A. Electronic structure: $(1\bar{1}0)$ surface

Figure 2(a) shows our calculated band structure of the un-optimized $(1\bar{1}0)$ slab. The surface Brillouin zone is shown as the inset of Fig. 2(b). The large residual forces are found at the z components of the atoms close to the surface and they are on the order of 1 eV/Å. The band structure does not show a well-defined Dirac cone in the vicinity of Γ and E_F. The Dirac-cone candidate bands have quadratic dispersion near Γ, and there are several bands bunched together right below E_F. The candidate bands for the lower Dirac cone have their charge densities strongly localized at the surface within three atomic layers, or 4.143 Å. This is different in character from the candidate band for the upper Dirac cone and implies that these bunched bands derive their surface state nature from the unrelaxed surface structure rather than a topological invariant. The inversion symmetry and time-reversal symmetry dictate that the band structure of the slab must have at least double degeneracy for all momenta.

Upon the geometry relaxation [Fig. 2(b)], a doubly degenerate Dirac cone near E_F is clearly identified, with the Dirac point located at Γ. The energy gap between the upper and lower Dirac cone is 3.2 meV at Γ due to the hybridization between the top and bottom surface states. Now the previously bunched bands right below E_F are shifted out of the bulk gap as expected. The decay length of both top-surface and bottom-surface Dirac states is about 30 Å, as shown in Fig. 2(c), which is about twice as long as that for the Bi$_2$Se$_3$ (111) surface. In both the upper and lower Dirac-cone surface states, Se contributions are dominant over Bi at a ratio of roughly 2.5:1, in contrast to the case of the (111) surface where Bi contributes more than Se at a ratio of 1.5:1 [24]. The dominant orbitals are p_x orbitals corresponding to p_z orbitals in the bulk crystal coordinates. Henceforth in this subsection, we discuss characteristics of the Dirac surface states for the optimized slab only.

The effective Hamiltonian for the p_x-dominated surface states localized at the $(1\bar{1}0)$ sur-
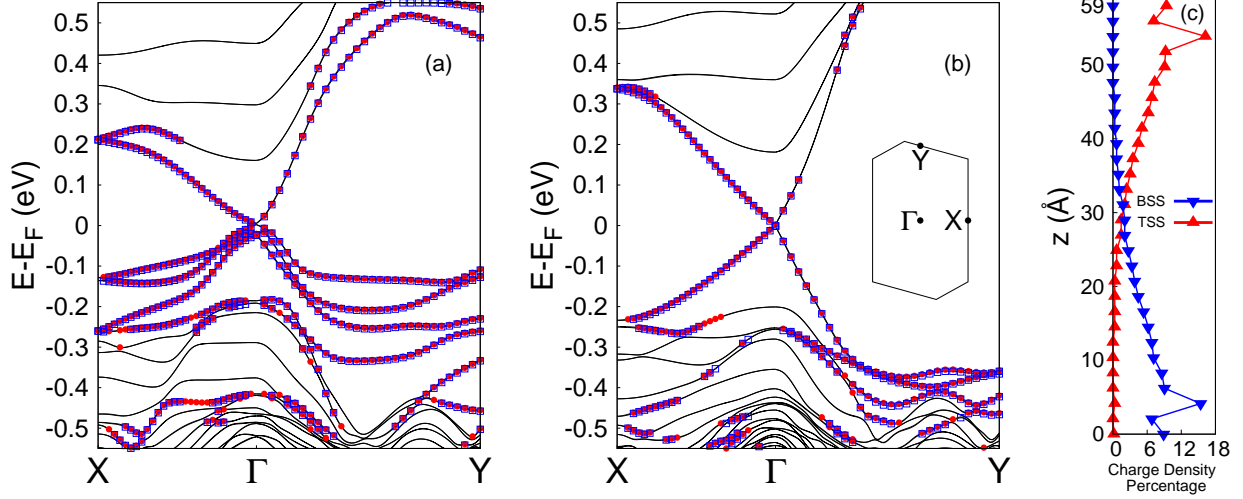
FIG. 2: (Color online) Band structures of (a) the un-optimized and (b) the optimized Bi_2Se_3 $(1\bar{1}0)$ slabs, where the top/bottom surface states are identified as circles/squares in red/blue. The Fermi level is zero in (a) and (b). (Inset) The surface-projected first Brillouin zone. (c) Charge density distributions vs vertical coordinate z for the top and bottom surface states in the optimized slab calculated near Γ (at $\vec{k} = (0.003, 0)$ $2\pi/a$ and 4.3 meV below the Dirac point), shown as red and blue, respectively.

face, in the vicinity of Γ, up to quadratic order is given by

$$\mathcal{H}_1(k) = E_0(k)I + [v_x k_x \sigma_y - v_y k_y \sigma_x] + \{\alpha_x k_x \sigma_x - \alpha_y k_y \sigma_y\} \tag{1}$$

where I is a 2×2 identity matrix, $E_0(k)$ contains a constant term and quadratic terms in k with effective masses, and v_x and v_y are the Fermi velocities along the x and y axes. This Hamiltonian satisfies time-reversal symmetry and the C_2 symmetry ($k_{x,y} \to -k_{x,y}$, $\sigma_{x,y} \to -\sigma_{x,y}$, and $\sigma_z \to \sigma_z$) of the $(1\bar{1}0)$ surface. The square-bracketed terms are Rashba-type SOC terms, and the braced terms are Dresselhaus-type SOC terms that are additionally allowed by the C_2 symmetry. Note that Rashba [25] and Dresselhaus [26] SOC terms are conventionally defined with isotropic coefficients such as $v_x = v_y$ and $\alpha_x = \alpha_y$.

The band structure, Fig. 2(b), and the constant energy contours, Fig. 3, unambiguously show strong anisotropy in the Fermi velocity. The Fermi velocities along the x and y axes would ordinarily be found by fitting the energy eigenvalues of the Dirac surface states in the small k region where only linear terms in k significantly contribute (0.0015 $2\pi/a \leq k \leq 0.015$ $2\pi/a$). The constant energy contours show that the ellipses have their principal

8

axes somewhat tilted from the x and y axes even for small k (the clockwise tilting angle of 16°), implying that the linear Rashba-type terms alone would incompletely describe the low-energy physics near Γ for this surface. Including the Dresselhaus-type terms in Eq. (1) gives rise to the tilting of the ellipse. These extra linear terms prevent us from extracting the Fermi velocities because the energy eigenvalues E_1 are

$$E_1 = E_0 + \frac{1}{2m_x^\star}k_x^2 + \frac{1}{2m_y^\star}k_y^2$$
$$\pm k\sqrt{u^2 \cos^2 \phi + q^2 \sin^2 \phi - 2r^2 \sin \phi \cos \phi}, \tag{2}$$
$$u^2 = v_x^2 + \alpha_x^2, \quad q^2 = v_y^2 + \alpha_y^2, \quad r^2 = v_y \alpha_x + v_x \alpha_y, \tag{3}$$

where E_0 is a constant term, $m_{x,y}^\star$ are the effective masses, and ϕ is an azimuthal angle in the $k_x - k_y$ plane measured counter-clockwise from the k_x-axis. Hence any fitting procedure will be unable to extract the set of four parameters, $\{v_x, v_y, \alpha_x, \alpha_y\}$, from just three equations. However, the u, q, and r values can be found from the fitting of the energy eigenvalues at several different values of ϕ. As evidenced by the energy contours, the ellipse for the lower Dirac cone is somewhat elongated in the major axis direction compared to the upper Dirac cone. This small particle-hole asymmetry leads to the u value being slightly larger for the unoccupied or upper Dirac cone than for the occupied or lower Dirac cone. Upon averaging the values of each parameter found from fitting at different values of ϕ and averaging across the upper and lower Dirac cones, we find that $u = 1.02\pm0.07$ eV·Å, $q = 2.35\pm0.03$ eV·Å, and $r = 1.20\pm0.03$ eV·Å, where the uncertainties are obtained by considering the small difference between the upper and lower Dirac cones. We can estimate the values of the Fermi velocities and Dresselhaus parameters appearing in Eq. (1) by making the assumption that the ratio of the Fermi velocities, (v_x/v_y), is the same as the ratio of the Dresselhaus parameters, (α_x/α_y). With this assumption, the values of the four parameters are as follows in units of eV·Å : $v_x = 0.97 \pm 0.10$, $v_y = 2.23 \pm 0.04$, $\alpha_x = 0.33 \pm 0.04$, and $\alpha_y = 0.74 \pm 0.07$.

B.   Spin and Spin-Orbital Textures: (1$\bar{1}$0) surface

Let us first discuss the in-plane spin texture of the Dirac surface states. The arrows in Fig. 3 show total in-plane spin textures at the constant energy contours for the upper and lower Dirac cones localized at the top surface that are obtained from spin expectation values of the DFT-calculated surface-state bands. To avoid effects of higher-order terms in k, the
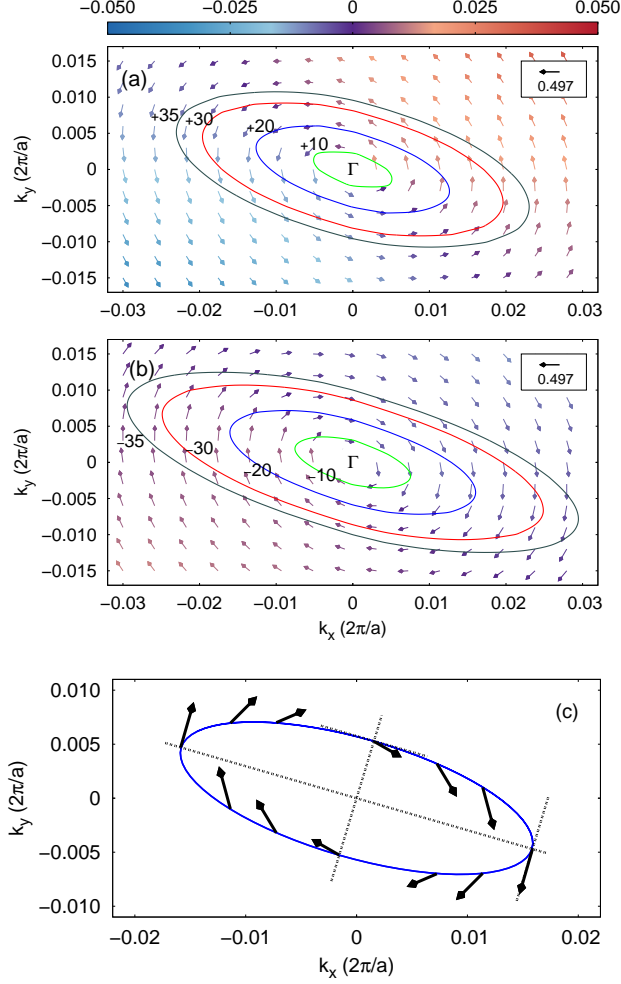
FIG. 3: (Color online) Spin-texture of the Dirac cone surface states localized at the top surface for the optimized ($1\bar{1}0$) slab at the constant energy contours. The length of the vectors indicates in-plane spin polarization, and out-of-plane spin polarization is indicated by the color scale. Constant energy contours corresponding to $\pm$ 10, 20, 30, and 35 meV with respect to the Dirac point (Fermi level) are overlaid in green, blue, red, and black, respectively. (a) The upper Dirac cone and (b) the lower Dirac cone. (c) A schematic representation of the in-plane spin directions along the -20 meV energy contour of the lower Dirac cone. The spins are calculated using DFT at points very near to the energy contour, and the principal axes are shown, as are the tangents to the energy contour at points along the principal axes.

spin textures are calculated close to the Dirac point. The total in-plane spin polarization is similar for both the upper and lower Dirac cones and reaches up to 0.51 μ_B, which is about a 25% increase compared to that in the (111) surface. The in-plane spin polarization rotates counter-clockwise (clock-wise) around the Γ point for the upper (lower) Dirac cone. Interestingly, the spin directions neither align parallel to the tangent to the constant energy contours nor obey perpendicular momentum-locking along the k_x and k_y axes, despite some similarity to Rashba-like features. Here the perpendicular spin-momentum locking means $\mathbf{s}_k \cdot \mathbf{k} = 0$, where $\mathbf{s}_k$ is an in-plane spin vector at in-plane momentum $\mathbf{k}$. To understand the origin of our calculated spin texture, we examine five representative cases: (i) $v_x \neq v_y$ and $\alpha_x = \alpha_y = 0$, (ii) $v_x = v_y$ and $\alpha_x = \alpha_y$, (iii) $v_x = v_y$ and $\alpha_x \neq \alpha_y$, (iv) $v_x \neq v_y$ and $\alpha_x = \alpha_y$, (v) $v_x \neq v_y$, $\alpha_x \neq \alpha_y$. Our analysis shows that the spin directions do not align tangent to the energy contours *away* from either the k_x and k_y axes or the principal axes when the contours are elliptic such as in all the five cases. However, the perpendicular spin-momentum locking still persists along either the k_x and k_y axes or the principal axes, only when the Fermi velocity is isotropic or there are no Dresselhaus-type terms, i.e., cases (i)-(iii). Therefore, we suggest that our calculated spin texture is attributed to a combined effect of anisotropic Fermi velocity with the Dresselhaus-type terms.

The detailed calculations of the implications of the calculated spin texture on transport properties are beyond the scope of this paper. There have been multiple studies of observations of spin accumulations of Bi_2Se_3 thin films driven by spin-unpolarized charge currents, especially when layered on a ferromagnetic material. [27, 28] Due to the traditional perpendicular spin-momentum locking associated with the surface states of the (111) slab, the spin accumulation direction was always perpendicular to the direction of the carrier momentum. If similar experiments are performed for this side surface, the observed spin accumulation direction may not be perpendicular to the carrier momentum direction.

Another noticeable effect is found in the in-plane spin-orbital texture. The arrows in Fig. 4(a)-(c) show p_x, p_y, and p_z orbital projections of the spin expectation values for the upper Dirac cone shown in Fig.3(a). The spin-orbital texture of the lower Dirac cone is opposite to that of the upper Dirac cone. We find that the p_x and p_z orbitals show the same spin circulation directions, whereas the spin expectation values arising from the p_y orbitals reveal Dresselhaus-like spin texture, i.e., rotates *away* from the Γ point. However, since the contribution of the p_x orbitals is dominant, the total spin texture follows that of the p_x

orbitals. The Se and Bi contributions to the spin textures are not the same as each other; aside from Se and Bi contributing to the spin polarization at a ratio of approximately 2.5:1, the spin directions from the Bi and Se sublattices are not parallel to each other for most ϕ values [Fig. 4(d)-(e)]. For the Bi sublattice the y components of spin are dominant in the plane, whereas for the Se sublattice there is no such tendency.

The color scale in Fig. 3 shows the total out-of-plane spin textures for the upper and lower Dirac cones localized at the top surface. For the out-of-plane spin component, we find that the spin polarization is greater than $0.01 \, \mu_B$ even at small k values on the order of $0.01 \, 2\pi/a$, where contributions of higher-order terms are expected to be negligible. The magnitude of out-of-plane spin polarization increases slowly with increasing k. Perfect C$_2$ symmetry combined with time-reversal symmetry does not allow an out-of-plane spin component from any order of the in-plane momenta in the effective Hamiltonian, Eq. (1). Therefore, the z component of spin must originate from slightly broken C$_2$ symmetry, which we find is attributed to the geometry optimization. For example, for the un-optimized ($1\bar{1}0$) slab which has perfect C$_2$ symmetry, the upper Dirac-cone candidate band does not have the z component of spin. Considering this observation, we expect that small linear terms such as $(\gamma_x k_x + \gamma_y k_y)\sigma_z$ are allowed upon the slightly broken C$_2$ symmetry. These additional linear terms would only affect the energy eigenvalues through modification of u^2 to $(v_x^2 + \alpha_x^2 + \gamma_x^2)$ and q^2 to $(v_y^2 + \alpha_y^2 + \gamma_y^2)$ without any change of r^2 in Eq. (3). Thus, the effect of γ_x and γ_y on the energy eigenvalues is evidently much less than that of α_x and α_y. Furthermore, since the values of γ_x and γ_y are expected to be much smaller than the values of α_x and α_y, in order to obtain the values of γ_x and γ_y from the fitting, the higher-order terms in the bulk Hamiltonian need to be included before rotations of the spatial and spin coordinates. This is beyond the scope of our current work. Notice that the spin and spin-orbital textures of the Dirac cones aforementioned in this subsection are opposite to those of the Dirac cones localized at the bottom surface in the sense that both the spin circulation directions and the out-of-plane spin polarization are opposite to each other. Therefore, the existence of the z component of spin does not break time-reversal symmetry in the slab because the z component of spin at a given k value localized at the top surface exactly cancels out with that localized at the bottom surface.

We now compare our calculated spin textures to those predicted by Refs. [16–18], where the ($1\bar{1}0$) and ($11\bar{2}$) surfaces are supposed to show identical spin textures, as previously stated

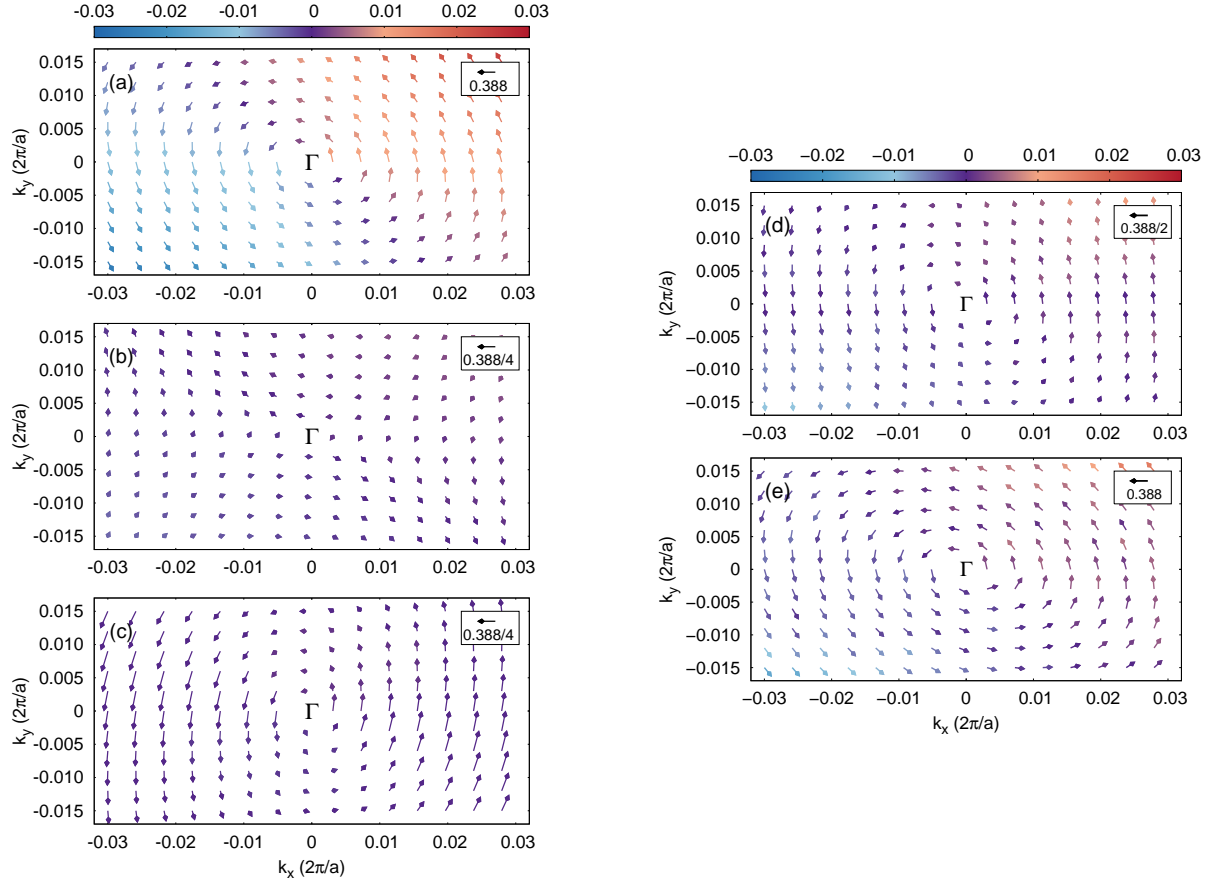FIG. 4: (Color online) Spin-orbital textures of the upper Dirac cone localized at the top surface for the $(1\bar{1}0)$ slab, projected onto the (a) p_x, (b) p_y, and (c) p_z orbitals. Note the in-plane scale for (a) differs from those for (b) and (c). Sublattice decomposed spin textures of the upper Dirac cone localized at the top surface: (d) Bi sublattice, and (e) Se sublattice. In (a)-(e) the color scales are for the out-of-plane spin component. Note the in-plane scale for (d) differs from that of (e).

in Sec.II. In the literature, the continuous rotational symmetry in the bulk Hamiltonian, enforced by keeping only linear and quadratic terms in k, dictates that the spin polarization be perpendicular to the mirror symmetry plane at un-tilted elliptic constant energy contours for all the surfaces normal to the (111) surface. In addition, the Se and Bi sublattices were assumed to equally contribute to the Dirac surface states. However, as shown in Fig. 1(b), the $(1\bar{1}0)$ surface does not have mirror symmetry. Instead it has C_2 symmetry about the z axis. Our DFT-calculated Dirac surface states form elliptic constant energy contours

tilted by about 16° from the k_x axis, and our DFT-calculated spin and spin-orbital textures completely differ from those of the literature. The surface reconstruction effect included in the DFT calculation is found to be important for Dirac surface states, although the geometry relaxation maintains the spatial symmetry to a high degree. The qualitative differences between our result and the literature are due to the fact that our DFT calculations capture the correct spatial symmetry and the surface reconstruction effect of the $(1\bar{1}0)$ surface, whereas the model Hamiltonian in the literature does not.

V.   RESULTS AND DISCUSSION FOR $(11\bar{2})$ SURFACE

A.   Electronic structure: $(11\bar{2})$ surface

Due to inversion symmetry and time-reversal symmetry, the band structure of the slab has at least double degeneracy for all momenta. At the time-reversal invariant momenta (X, Y, and Γ in the inset of Fig. 5) the bands have fourfold degeneracy. Similarly to the $(1\bar{1}0)$ slab, we first compare the band structures of the un-optimized and optimized $(11\bar{2})$ slabs, as shown in Fig. 5(a) and (b), respectively. The surface Brillouin zone is shown as the inset of Fig. 5(b). The un-optimized slab has large residual forces on the atoms close to the top and bottom surfaces and the maximum force is on the order of 1 eV/Å. The band structure of the un-optimized slab does not clearly show Dirac cones near Γ, despite Dirac-like cones at the Y point. The bands crossing the Fermi level at Γ quickly flatten out and group with other bands as k increases. Henceforth, we consider only the optimized slab.

1.   Near the Γ point

The band structure of the optimized $(11\bar{2})$ slab is distinct from those of the $(1\bar{1}0)$ and (111) slabs in many ways, although the $(11\bar{2})$ slab holds topological surface states, as it should in the presence of time-reversal symmetry. The complexity of the band structure of the $(11\bar{2})$ slab in relation to those of the $(1\bar{1}0)$ and (111) slabs is likely influenced by the lower symmetry and the presence of twelve broken covalent bonds, whereas there are only eight broken covalent bonds in the $(1\bar{1}0)$ surface and zero in the (111) surface (due to the van der Waals coupled quintuple layers along the crystal c-axis). Let us first discuss the upper and lower Dirac cones near E_F with the Dirac point at Γ, as shown in Fig. 5(b). The Dirac point
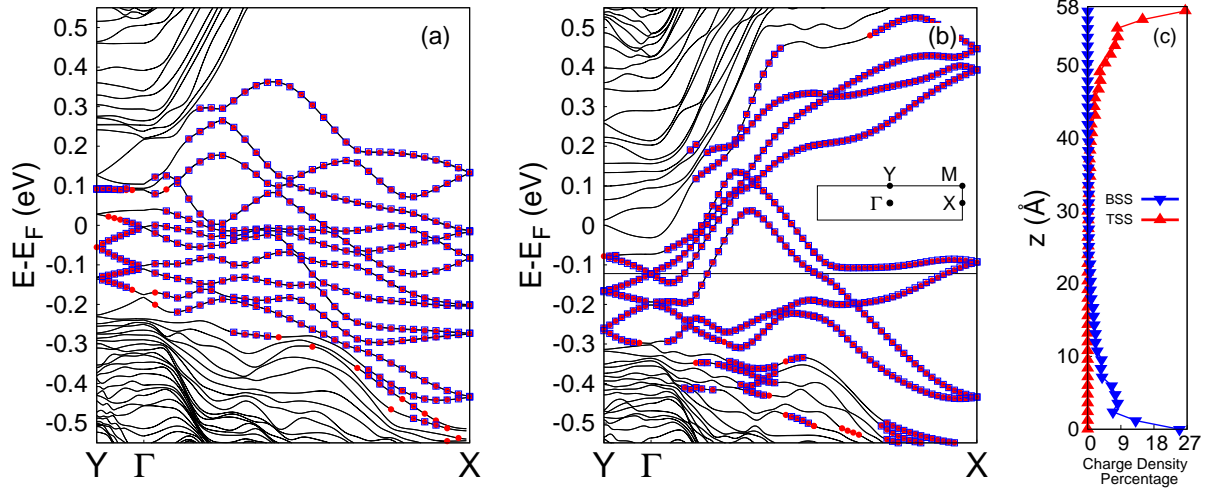
FIG. 5: (Color online) Band structures of (a) the unoptimized and (b) the optimized Bi_2Se_3 $(11\bar{2})$ slabs, where the top/bottom surface states are identified as circles/squares in red/blue. The horizontal line is to guide the eye at $E_\Gamma^{DP} = -0.12$ eV. (Inset) The surface first Brillouin zone for the $(11\bar{2})$ slab. (c) Charge density distributions vs vertical coordinate z for the top and bottom surface states in the optimized slab calculated near Γ (at $\vec{k} = (0.009, 0)$ $2\pi/a$ and 8.7 meV below the Dirac point), shown as red and blue, respectively.

at Γ, E_Γ^{DP}, is located at 0.12 eV below E_F, due to the surface potential. This indicates that the surface reconstruction effect is significant, although the $(11\bar{2})$ surface is non-polar. The energy gap between the upper and lower Dirac cones is 1.4 meV caused by the small surface hybridization. The decay length of the surface states is about 15 Å, which is much shorter than the $(1\bar{1}0)$ surface but comparable to that for the (111) surface [Fig. 5(c)]. The p_y orbital dominantly contributes to the surface states. Similarly to the $(1\bar{1}0)$ slab, Se contributions are dominant over Bi contributions at a ratio of 2.5:1 for both the upper and lower Dirac cones.

Considering the symmetries of the $(11\bar{2})$ surface, the effective Hamiltonian for the p_y-dominated surface states up to quadratic order, in the vicinity of E_Γ^{DP}, is given by

$$\mathcal{H}_2(k) = E_0(k)I + [v_x k_x \sigma_y - v_y k_y \sigma_x] + \{\gamma k_x \sigma_z\}, \tag{4}$$

where the braced term is an additional linear term allowed by the mirror symmetry of the $(11\bar{2})$ surface about the y axis ($k_x \to -k_x$, $k_y \to k_y$, $\sigma_x \to \sigma_x$, and $\sigma_{y,z} \to -\sigma_{y,z}$).

Figure 6 (c) and (d) show our calculated constant energy contours above and below E_Γ^{DP},

respectively, for the states localized at the top surface. At low energies or energies up to 10 meV above or below the Dirac point, the contours are vertically elongated ellipses for both the upper and lower Dirac cones. However, at high energies or energies sufficiently away from the Dirac point, the size and shape of the contours for the upper Dirac cone differ from those for the lower Dirac cone. The upper Dirac cone starts to have rectangular-shaped contours from 15 meV above the Dirac point, while the lower Dirac cone retains the same elliptic shape. Therefore, in the case of low energies we fit our DFT-calculated surface-state bands to the energy eigenvalues as a function of k and ϕ for $0.0015\,2\pi/a \leq |k| \leq 0.015\,2\pi/a$, with two parameters $s \equiv \sqrt{v_x^2 + \gamma^2}$ and v_y. The energy eigenvalues E_2 of Eq. (4) are

$$E_2 \;=\; E_0 + \frac{1}{2m_x^\star}k_x^2 + \frac{1}{2m_y^\star}k_y^2 \pm k\sqrt{s^2\cos^2\phi + v_y^2\sin^2\phi}. \tag{5}$$

Upon averaging the values of each parameter found from fitting at different values of ϕ and averaging across the upper and lower Dirac cones, we find that $s = 0.69 \pm 0.07$ eV·Å and $v_y = 0.53 \pm 0.05$ eV·Å. This fitting result is consistent with our DFT-calculated energy contours at low energies. We cannot separately obtain the values of v_x and γ unless the out-of-plane spin polarization is fitted. However, as will be discussed in Sec.V.B.1, we cannot perform a quantitative fitting of the out-of-plane spin polarization based on Eq. (4) due to the complex spin texture.

2. Other than the Γ point

In addition to the Dirac point at Γ, we find a pair of Dirac cones slightly above and below E_Γ^{DP} at the Y point and multiple crossings of the surface states between Γ and X near E_F, as shown in Fig. 5(b). All of the identified surface states appearing not near Γ, also have a decay length comparable to those near Γ, as shown in Fig. 5(c). The Dirac points at Y with energies of 0.08 eV and 0.17 eV below E_F are referred to as $E_{Y,\mathrm{high}}^{\mathrm{DP}}$ and $E_{Y,\mathrm{low}}^{\mathrm{DP}}$, respectively. The energy gaps at the former and latter Dirac points are 2.6 meV and 1.8 meV, respectively. The crossings of the states at X and $(k_x, k_y) = (0.318, 0)\,2\pi/a$ (around 0.20 eV below E_F) are not associated with Dirac cones because their dispersion relations are essentially flat rather than linear along the k_y axis (not shown).

Figures 6(b), (e), and (f) show constant energy contours of the states localized at the top surface below $E_{Y,\mathrm{high}}^{\mathrm{DP}}$ and above and below $E_{Y,\mathrm{low}}^{\mathrm{DP}}$ at the Y point, respectively. The flat Dirac
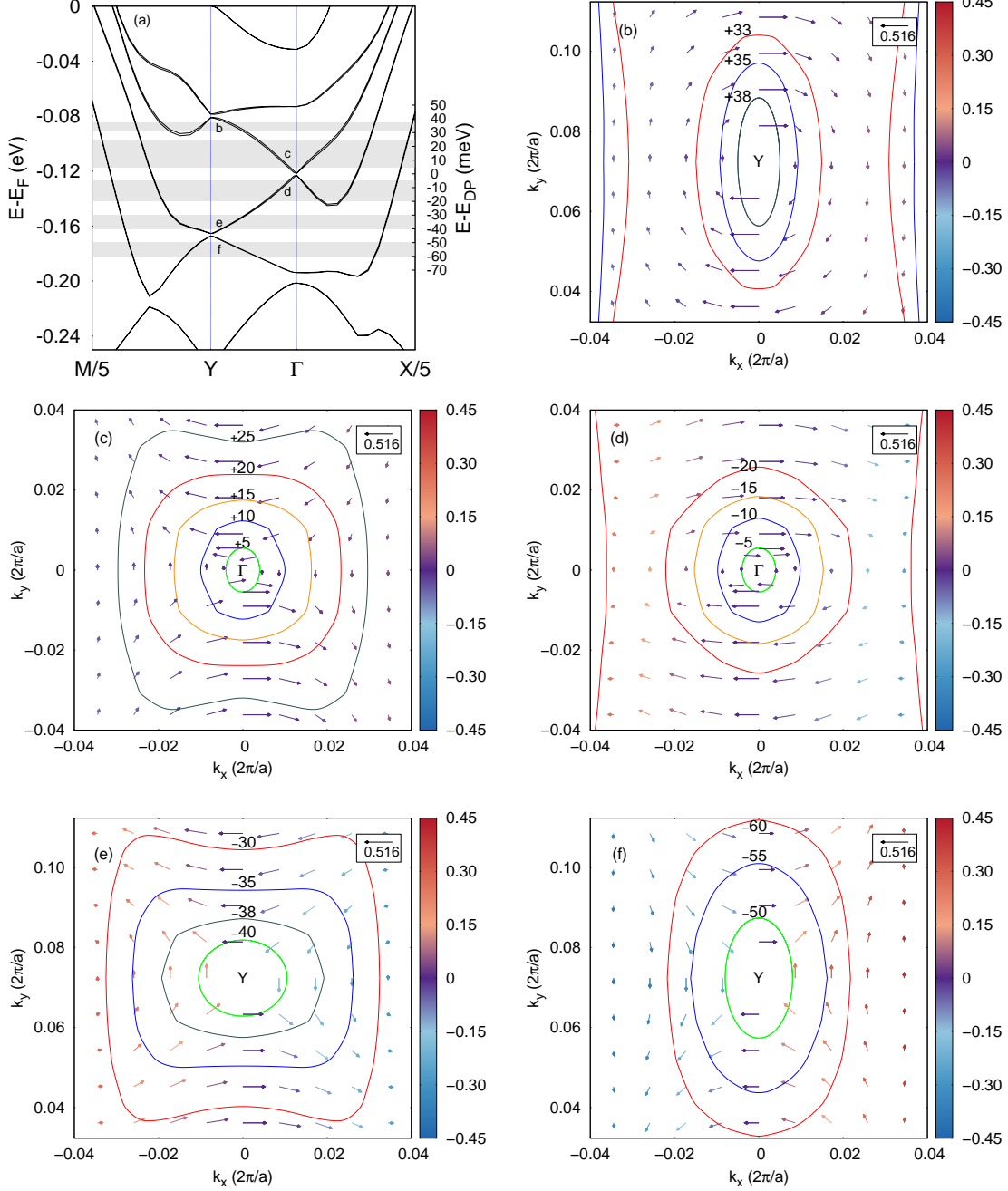
FIG. 6: (Color online) (a) Band structure centered about the Dirac point at Γ and the two Dirac points at Y. Regions from which constant energy contours are drawn are shown in gray, along with the corresponding figure label. (b-f) Total in-plane and out-of-plane spin textures at constant energy contours for the states localized at the top surface of the optimized $(11\bar{2})$ slab: (b) the lower Dirac cone at $E_{\mathrm{Y,high}}^{\mathrm{DP}}$, (c) the upper Dirac cone at Γ, (d) the lower Dirac cone at Γ, (e) the upper Dirac cone at $E_{\mathrm{Y,low}}^{\mathrm{DP}}$, and (f) the lower Dirac cone at $E_{\mathrm{Y,low}}^{\mathrm{DP}}$. In (b)-(f) the numbers at the contours indicate energies relative to the Dirac point at Γ, and the arrows at the contours and the color scale represent the in-plane and out-of-plane spin components, respectively.

cone above $E^{\mathrm{DP}}_{Y,\mathrm{high}}$ prevents us from obtaining energy contours. Now at about 10 meV or farther away from $E^{\mathrm{DP}}_{Y,\mathrm{low}}$, the energy contours of the upper Dirac cone noticeably differ from those of the lower Dirac cone. The upper Dirac cone has horizontally elongated elliptic or rectangular contours, whereas the lower Dirac cone has vertically elongated elliptic contours.

B.   Spin and Spin-Orbital Textures: (11$\bar{2}$) surface

1.   Near the Γ point

We first present our analysis of the spin texture of the upper and lower Dirac cones localized at the top surface near Γ, as shown in Figs. 6(c) and (d). This spin texture is opposite to that of the Dirac cones localized at the bottom surface. Overall, the spin textures of both Dirac cones reveal dominant x components of spin for $|k_x| < 0.02\ 2\pi/a$. Along the k_y axis ($k_x = 0$) the spin is polarized along the x axis with the magnitude 0.52 μ_B at $k_y = 0.009\ 2\pi/a$ and it increases to 0.54 μ_B at $k_y = 0.063\ 2\pi/a$. However, there is a fundamental difference in the spin texture between the upper and lower Dirac cones. For the upper Dirac cone the spin polarization circulates clockwise around the Y point (Dresselhaus-like), whereas for the lower Dirac cone the spin rotates again clockwise around the Γ point. This difference has not been observed for the (111) and (1$\bar{1}$0) surfaces. Compare Fig. 6(c) to Fig. 3(a). For $|k_x| > 0.02\ 2\pi/a$, along the k_x axis, the in-plane spin polarization of both Dirac cones becomes very small.

For a better understanding of the aforementioned spin texture, we examine the spin polarization projected onto the p_x, p_y, and p_z orbitals for each cone, as shown in Fig. 7. For both Dirac cones the p_y orbital contributes most to the spin texture, while the p_x orbital contributes least. The different in-plane spin circulations for the upper and lower Dirac cones are clearly shown in the p_y orbital projection. However, that is not the case for the p_x and p_z orbital projections. Interestingly, the p_z-orbital projection shows the spin circulation around the Y point (Dresselhaus-like) for both the upper and lower Dirac cones, whereas the p_x-orbital projection reveals the circulation around the Γ point (Rashba-like). Along the k_y axis the spin polarizations of the p_y and p_z orbitals are opposite to that of the p_x orbital. Additionally, we separate the spin polarization of the Bi atoms from that of the Se atoms, as shown in Fig. 8. The contribution of the Se atoms is greater than that of the Bi atoms. The

Se sublattice shows the spin circulating around the Y (Γ) point for the upper (lower) Dirac cone, just like the total spin polarization. But the Bi sublattice reveals the spin winding around the Y point (Dresselhaus-like) for both the upper and lower Dirac cones.

In addition to the in-plane spin polarization, our DFT calculation shows a small out-of-plane spin polarization on the order of 0.01 μ_B even near Γ that is apparent from the color scale of Figs. 7 and 8. The out-of-plane spin component appears in the whole plane except for the k_y axis. This is consistent with the reasoning that the out-of-plane spin polarization arises from the $\gamma k_x \sigma_z$ term in Eq. (4). An estimate of this term from the fitting of our DFT-calculated spin expectation values is not feasible due to the aforementioned complex dependence of the total spin polarization on k and ϕ.

We now briefly mention the comparison of our result to the prediction made by Refs.[16–18]. The prediction states that for any normal surface the spin polarization is strictly perpendicular to the [111] direction and it is in the surface plane at un-rotated elliptic constant energy contours. Refs.[17, 18] suggest that the Bi sublattice gives rise to the Rashba spin texture and the Se sublattice the Dresselhaus spin texture, which does not agree with our DFT result for the upper Dirac cone and is opposite to that for the lower Dirac cone. If the Bi and Se sublattices contribute equally, the prediction in Ref.[16] agrees with that in Refs.[17, 18]. Hence, the result in Refs.[16–18] captures only the overall feature of the in-plane spin polarization of our DFT-calculated Dirac surface states near Γ for the $(11\bar{2})$ surface. The literature could not predict the additional Dirac points at the Y point. Note that the Hamiltonian used in the literature and Eq. (4) have mirror symmetry, while Eq. (1) does not. The absence of mirror symmetry in the $(1\bar{1}0)$ surface makes the prediction of the literature inapplicable to the $(1\bar{1}0)$ surface.

2. Near the Y point

We discuss the spin and spin-orbital textures of the Dirac cones localized at the top surface near the Y point. The arrows in Fig. 6(b), (e), and (f) show the spin textures of the lower Dirac cone at $E_{Y,\text{high}}^{\text{DP}}$ and the upper and lower Dirac cones at $E_{Y,\text{low}}^{\text{DP}}$, respectively. The former lower Dirac cone circulates clockwise around the Y point with dominant x components of spin along the k_y axis, similarly to the lower Dirac cone at the Γ point. Immediately away from the k_y axis, the spin polarization of this band is greatly reduced. The spin texture of
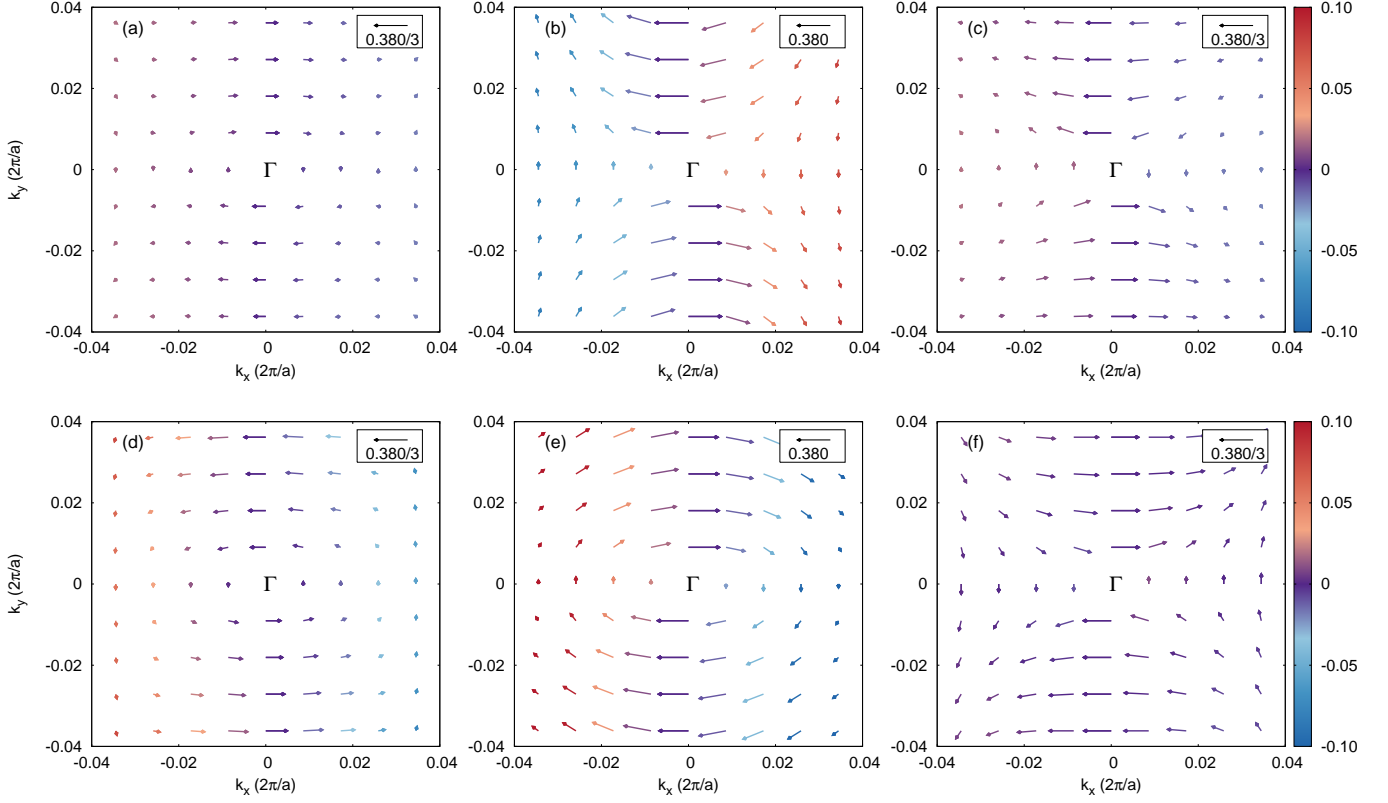
FIG. 7: (Color online) Orbitally decomposed spin textures of (a-c) the upper Dirac cone and (d-f) the lower Dirac cone of the surface states localized at the top surface near Γ for the $(11\bar{2})$ slab shown in Fig. 6(c,d); (a) and (d) for the p_x orbital, (b) and (e) for the p_y orbital, and (c) and (f) for the p_z orbital. The in-plane spin polarization is given by the magnitude of the arrows, and the out-of-plane spin polarization is given by the color-scale. Note the different in-plane scale in (b) and (e) for the p_y orbital from the other in-plane scales.

the upper Dirac cone at $E_{Y,\text{high}}^{\text{DP}}$ is not obtained since it is difficult to assign constant energy contours due to the flatness of the cone. Now regarding the Dirac cones at $E_{Y,\text{low}}^{\text{DP}}$, the spin at the k_y axis is polarized along the x axis with the magnitude 0.33 μ_B at $k_y = 0.063\ 2\pi/a$ about the Y point. However, right away from the k_y axis, unexpectedly, their spin textures are distinct from those of the Dirac cones at Γ in two ways. Compare Fig. 6(c) and (d) to (e) and (f). The first feature is that both the upper and lower Dirac cones now circulate around Γ, similar to the Dresselhaus-type spin texture. The spin polarization of the upper (lower) cone rotates clockwise (counter-clockwise) relative to the Γ point. The second feature is
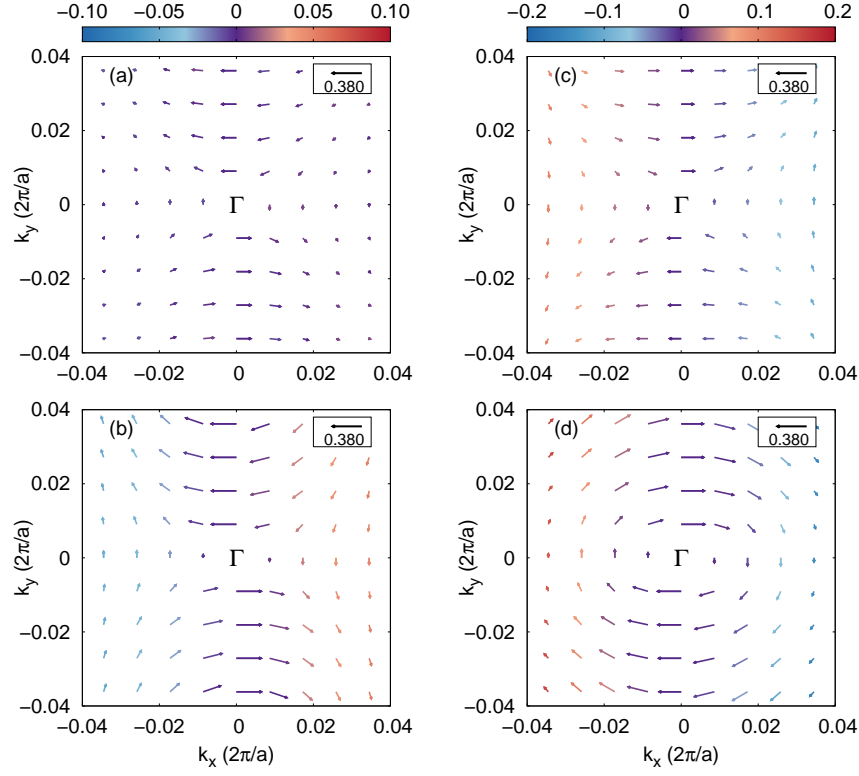
20

FIG. 8: (Color online) Sublattice decomposed spin textures of (a,b) the upper Dirac cone and (c,d) the lower Dirac cone of the surface states shown in Fig. 6(c,d): (a,c) Bi sublattice and (b,d) Se sublattice. The meanings of the in-plane and out-of-plane spin polarization scales are the same as those in Fig. 7.

that there is a significant out-of-plane spin polarization except for the k_y axis, at least one order of magnitude greater than that of the Dirac cones near Γ.

To understand these features near $E_{Y,\text{low}}^{\text{DP}}$ at Y, we calculate the spin-orbital texture and Bi and Se sublattice contributions. Figure 9(a-c) show the spin polarization projected onto the p_x, p_y, and p_z orbitals of the lower Dirac cone at $E_{Y,\text{low}}^{\text{DP}}$. The p_y orbital contributes most to the spin polarization. The spin polarization arising from the p_y orbitals circulates counter-clockwise around Γ and it has also a significant out-of-plane component. The p_y- and p_z-orbital spin projections are opposite to the p_x-orbital contribution. Both p_y and p_z orbitals show the Dresselhaus-like spin texture. The spin-orbital texture of the upper Dirac cone (not shown) is opposite to that of the lower Dirac cone. Figure 9(d-e) shows the Bi and Se sublattice contributions to the spin texture for the lower Dirac cone. In this case, both
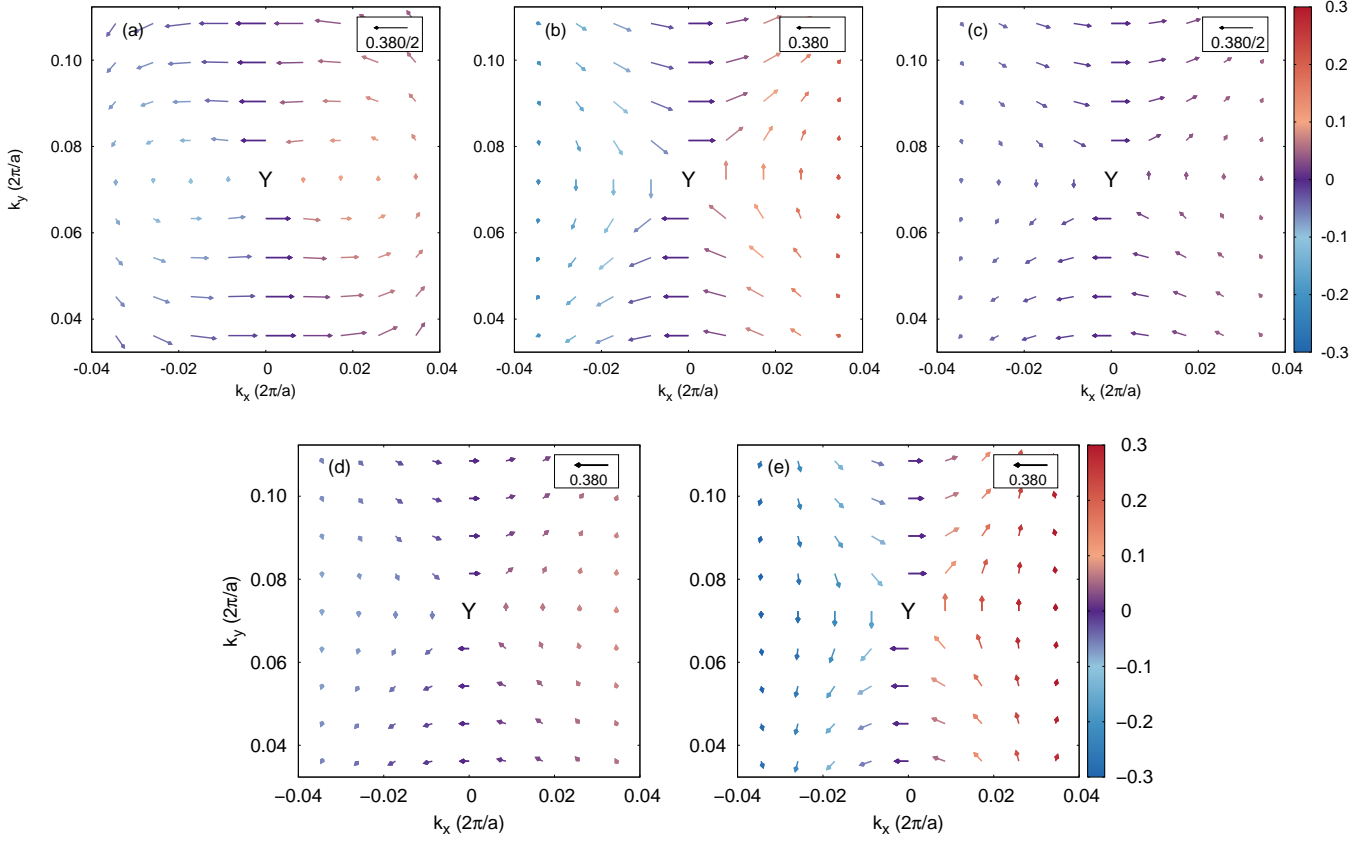
21

FIG. 9: (Color online) Orbitally decomposed spin textures of (a-c) the lower Dirac cone of the surface state localized at the top surface near $E_{Y,\text{low}}^{\text{DP}}$ shown in Fig. 6(f): (a) the p_x orbital, (b) the p_y orbital, and (c) the p_z orbital. (d,e) Bi and Se sublattice decomposed spin textures of the lower Dirac cone near the Y point, respectively. The meanings of the in-plane and out-of-plane spin polarization scales are the same as those in Fig. 7. The scales of the arrows in (a) and (c) are different from those in (b), (d), and (e).

the Bi and Se sublattices reveal the circulations of the spin around Γ or the Dresselhaus-like SOC feature about Y.

VI. CONCLUSION

We have investigated the spin and spin-orbital textures and electronic structures of the topological surface states of two representative normal surfaces to the (111) surface, such as $(1\bar{1}0)$ and $(11\bar{2})$ surfaces, by using relaxed slabs constructed within DFT. In addition to

inversion and time-reversal symmetries, the $(1\bar{1}0)$ surface has C_2 symmetry and the $(11\bar{2})$ surface has mirror symmetry. Effects of different surface symmetries and surface reconstruction were included in our DFT calculations of the slabs, in contrast to the effective model Hamiltonian approach based on linear and quadratic terms in momentum. This difference produces qualitative discrepancy between our findings and the results of the model Hamiltonian approach. We found that the spin and spin-orbital textures of the Dirac cones for the two normal surfaces entirely differ from each other and from those for the (111) surface. Interestingly, the $(1\bar{1}0)$ surface shows a combination of Rashba-type and Dresselhaus-type spin texture, and the spin directions do not align tangent to the tilted elliptic constant energy contours. For the $(11\bar{2})$ surface, the upper and lower Dirac cones near Γ shows the Dresselhaus-like and Rashba-like spin textures, respectively, whereas both Dirac cones near the Y point have the Dresselhaus-like spin texture.

Acknowledgments

[1] M. Z. Hasan and C. L. Kane, Rev. Mod. Phys. **82**, 3045 (2010).

[2] X.-L. Qi and S.-C. Zhang, Rev. Mod. Phys. **83**, 1057 (2011).

[3] L. Fu, Phys. Rev. Lett. **106**, 106802 (2011).

[4] H. Zhang, C.-X. Liu, X.-L. Qi, X. Dai, Z. Fang, and S.-C. Zhang, Nature Phys. **5**, 438 (2009).

[5] H. Zhang, C.-X. Liu, and S.-C. Zhang, Phys. Rev. Lett. **111**, 066801 (2013).

[6] Z.-H. Zhu, C. N. Veenstra, G. Levy, A. Ubaldini, P. Syers, N. P. Butch, J. Paglione, M. W. Haverkort, I. S. Elfimov, and A. Damascelli, Phys. Rev. Lett. **110**, 216401 (2013).

[7] A. T. Lee, M. J. Han, and K. Park, Phys. Rev. B **90**, 155103 (2014).

[8] L. Miao, Z. F. Wang, M.-Y. Yao, F. Zhu, J. H. Dil, C. L. Gao, C. Liu, F. Liu, D. Qian, J.-F.

Jia, Phys. Rev. B **89**, 155116 (2014).

[9] H. Peng, K. Lai, D. Kong, S. Meister, Y. Chen, X.-L. Qi, S.-C. Zhang, Z.-X. Shen, and Yi Cui, Nat. Mat. **9**, 225 (2009).

[10] D. Kong, W. Dang, J. J. Cha, H. Li, S. Meister, H. Peng, Z. Liu, and Y. Cui, Nano Lett. **10**, 2245 (2010).

[11] Y. Zou, Z.-G. Chen, Y. Huang, L. Yang, J. Drennan, and J. Zou, J. Phys. Chem. C **118**, 20620 (2014).

[12] L. A. Jauregui, M. T. Pettes, L. P. Rokhinson, L. Shi, and Y. P. Chen, Sci. Rep. **5**, 8452 (2015).

[13] A. Zhuang, J.-J. Li, Y.-C. Wang, X. Wen, Y. Lin, B. Xiang, X. Wang, and J. Zeng, Angew. Chem. Int. Ed. **53**, 6425 (2014).

[14] C.-Y. Moon, J. Han, H. Lee, and H. J. Choi, Phys. Rev. B **84**, 195425 (2011).

[15] Z. Xu, X. Guo, M. Yao, H. He, L. Miao, L. Jiao, H. Liu, J. Wang, D. Qian, J. Jia, W. Ho, and M. Xie, Adv. Mat. **25**, 1557 (2013).

[16] F. Zhang, C. L. Kane, and E. J. Mele, Phys. Rev. B **86**, 081303(R) (2012).

[17] P. G. Silvestrov, P. W. Brouwer, and E. G. Mishchenko, Phys. Rev. B **86**, 075302 (2012).

[18] P.-H. Chang, F. Mahfouzi, N. Nagaosa, and B. K. Nikolić, Phys. Rev. B **89**, 195418 (2014).

[19] K. Momma and F. Izumi, J. Appl. Crystallogr. **44**, 1272-1276 (2011).

[20] S. Nakajima, J. Phys. Chem. Sol. **24**, 479 (1963).

[21] G. Kresse and D. Joubert, Phys. Rev. B **59**, 1758 (1999).

[22] J. P. Perdew, K. Burke, and M. Ernzerhof, Phys. Rev. Lett. **77**, 3865 (1996).

[23] P. E. Blöchl, Phys. Rev. B **50**, 17953 (1994).

[24] K. Park, C. De Beule, and B. Partoens, New J. Phys. **15**, 113031 (2013).

[25] Y. A. Bychkov and E. I. Rashba, JETP Lett. **39**, 78 (1984).

[26] G. Dresselhaus, Phys. Rev. **100**, 580 (1955).

[27] A. R. Mellnik, J. S. Lee, A. Richardella, J. L. Grab, P. J. Mintun, M. H. Fischer, A. Vaezi, A. Manchon, E.-A. Kim, N. Samarth, Nature **511** 449 (2014).

[28] C. H. Li, O. M. J. van 't Erve, J. T. Robinson, Y. Liu, L. Li, B. T. Jonker, Nature Nanotech. **9** 218 (2014).